

# Measurement bias in self-heating x-ray free electron laser experiments from diffraction studies of phase transformation in titanium






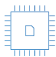
O. B. Ball ; R. J. Husband ; J. D. McHardy ; M. I. McMahon ; C. Strohm ; Z. Konôpková ; K. Appel ; V. Cerantola ; A. L. Coleman ; H. Cynn ; A. Dwivedi ; A. F. Goncharov ; H. Graafsma ; L. Q. Huston ; H. Hwang ; J. Kaa ; J.-Y. Kim ; E. Koemets; T. Laurus; X. Li ; H. Marquardt ; A. S. J. Méndez ; S. Merkel ; A. Mondal ; G. Morard ; V. B. Prakapenka ; C. Prescher ; T. R. Preston ; S. Speziale ; S. Stern; B. T. Sturtevant ; J. Sztuk-Dambietz; N. Velisavljevic ; C.-S. Yoo; U. Zastraun ; Zs. Jenei ; H. P. Liermann ; R. S. McWilliams 



J. Appl. Phys. 136, 115902 (2024)


<https://doi.org/10.1063/5.0215908>



 Nanotechnology & Materials Science  Optics & Photonics  Impedance Analysis  Scanning Probe Microscopy  Sensors  Failure Analysis & Semiconductors

Unlock the Full Spectrum.  
From DC to 8.5 GHz.  
Your Application. Measured.

[Find out more](#)














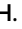















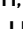
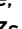




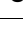
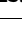
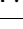
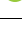
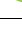
# Measurement bias in self-heating x-ray free electron laser experiments from diffraction studies of phase transformation in titanium

Cite as: *J. Appl. Phys.* **136**, 115902 (2024); doi: [10.1063/5.0215908](https://doi.org/10.1063/5.0215908)

Submitted: 26 April 2024 · Accepted: 31 May 2024 ·

Published Online: 19 September 2024



O. B. Ball,<sup>1</sup>  R. J. Husband,<sup>2</sup>  J. D. McHardy,<sup>1</sup>  M. I. McMahon,<sup>1</sup>  C. Strohm,<sup>2</sup>  Z. Konôpková,<sup>3</sup>   
K. Appel,<sup>3</sup>  V. Cerantola,<sup>3,4</sup>  A. L. Coleman,<sup>5</sup>  H. Cynn,<sup>5</sup>  A. Dwivedi,<sup>3</sup>  A. F. Goncharov,<sup>6</sup>  H. Graafsma,<sup>2</sup>   
L. Q. Huston,<sup>7</sup>  H. Hwang,<sup>2,8</sup>  J. Kaa,<sup>3,9</sup>  J.-Y. Kim,<sup>10</sup>  E. Koemets,<sup>11</sup>  T. Laurus,<sup>2</sup>  X. Li,<sup>2,12</sup>  H. Marquardt,<sup>11</sup>   
A. S. J. Méndez,<sup>2</sup>  S. Merkel,<sup>13</sup>  A. Mondal,<sup>14</sup>  G. Morard,<sup>15,16</sup>  V. B. Prakapenka,<sup>17</sup>  C. Prescher,<sup>2,18</sup>   
T. R. Preston,<sup>3</sup>  S. Speziale,<sup>19</sup>  S. Stern,<sup>2,20</sup>  B. T. Sturtevant,<sup>7</sup>  J. Sztuk-Dambietz,<sup>3</sup>  N. Velisavljevic,<sup>5</sup>   
C.-S. Yoo,<sup>21</sup>  U. Zastra,<sup>3</sup>  Zs. Jenei,<sup>5</sup>  H. P. Liermann,<sup>2,a)</sup>  and R. S. McWilliams<sup>1,b)</sup> 

## AFFILIATIONS

<sup>1</sup>The School of Physics and Astronomy, Centre for Science at Extreme Conditions, and SUPA, University of Edinburgh, Peter Guthrie Tait Road, Edinburgh EH9 3FD, United Kingdom

<sup>2</sup>Deutsches Elektronen-Synchrotron DESY, Notkestr. 85, 22607 Hamburg, Germany

<sup>3</sup>European XFEL, Holzkoppel 4, 22869 Schenefeld, Germany

<sup>4</sup>Department of Earth and Environmental Sciences (DISAT), University of Milano-Bicocca, Piazza della Scienza 4, 20126 Milan, Italy

<sup>5</sup>Lawrence Livermore National Laboratory, 7000 East Avenue, Livermore, California 94550, USA

<sup>6</sup>Carnegie Science, Earth and Planets Laboratory, 5241 Broad Branch Road, NW, Washington, DC 20015, USA

<sup>7</sup>Los Alamos National Laboratory, Los Alamos, New Mexico 87545, USA

<sup>8</sup>School of Earth Sciences and Environmental Engineering, Gwangju Institute of Science and Technology, 123 Cheomdan-Gwagiro, Gwangju 61005, Republic of Korea

<sup>9</sup>Fakultät Physik/DELTA, Technische Universität Dortmund, Maria-Goeppert-Mayer-Straße 2, Dortmund 44227, Germany

<sup>10</sup>Department of Physics, Research Institute for High Pressure, Hanyang University, 222 Wangsimni-ro, Seoul 04763, Republic of Korea

<sup>11</sup>Department of Earth Sciences, University of Oxford, South Parks Road, Oxford OX1 3AN, United Kingdom

<sup>12</sup>College of Physics, State Key Laboratory of Superhard Materials, Jilin University, Changchun 130012, China

<sup>13</sup>Univ. Lille, CNRS, INRAE, Centrale Lille, UMR 8207—UMET—Unité Matériaux et Transformations, F-59000 Lille, France

<sup>14</sup>Institut für Mineralogie, Universität Münster, Corrensstraße 24, D-48149 Münster, Germany

<sup>15</sup>Inst. Minéralogie, de Physique des Matériaux et de Cosmochimie (IMPMP), Sorbonne Université, UMR CNRS 7590, Museum National d'Histoire Naturelle, 4 Place Jussieu, Paris, France

<sup>16</sup>Université Grenoble Alpes, Université Savoie Mont Blanc, CNRS, IRD, IFSTTAR, ISTERRE, 38000 Grenoble, France

<sup>17</sup>Center for Advanced Radiation Sources, University of Chicago, Chicago, Illinois 60637, USA

<sup>18</sup>Institute of Earth and Environmental Sciences (Geomaterials and Crystalline Materials), Albert-Ludwigs-University Freiburg, Freiburg, Germany

<sup>19</sup>GFZ German Research Centre for Geosciences, Telegrafenberg, 14473 Potsdam, Germany

<sup>20</sup>X-Spectrum GmbH, Luruper Hauptstraße 1, 22547 Hamburg, Germany

<sup>21</sup>Department of Chemistry and Institute for Shock Physics, Washington State University, Pullman, Washington 99164, USA

<sup>a)</sup>Electronic mail: [hanns-peter.liermann@desy.de](mailto:hanns-peter.liermann@desy.de)

<sup>b)</sup>Author to whom correspondence should be addressed: [rs.mcwilliams@ed.ac.uk](mailto:rs.mcwilliams@ed.ac.uk)

19 September 2024 13:20:56

**ABSTRACT**

X-ray self-heating is a common by-product of X-ray Free Electron Laser (XFEL) techniques that can affect targets, optics, and other irradiated materials. Diagnosis of heating and induced changes in samples may be performed using the x-ray beam itself as a probe. However, the relationship between conditions created by and inferred from x-ray irradiation is unclear and may be highly dependent on the material system under consideration. Here, we report on a simple case study of a titanium foil irradiated, heated, and probed by a MHz XFEL pulse train at 18.1 keV delivered by the European XFEL using measured x-ray diffraction to determine temperature and finite element analysis to interpret the experimental data. We find a complex relationship between apparent temperatures and sample temperature distributions that must be accounted for to adequately interpret the data, including beam averaging effects, multivalued temperatures due to sample phase transitions, and jumps and gaps in the observable temperature near phase transformations. The results have implications for studies employing x-ray probing of systems with large temperature gradients, particularly where these gradients are produced by the beam itself. Finally, this study shows the potential complexity of studying nonlinear sample behavior, such as phase transformations, where biasing effects of temperature gradients can become paramount, precluding clear observation of true transformation conditions.

© 2024 Author(s). All article content, except where otherwise noted, is licensed under a Creative Commons Attribution (CC BY) license (<https://creativecommons.org/licenses/by/4.0/>). <https://doi.org/10.1063/5.0215908>

**I. INTRODUCTION**

In recent years, there have been an increasing number of extreme conditions and high-temperature experiments at X-ray free electron laser (XFEL) facilities using x rays to both probe and heat samples.<sup>1–8</sup> Volumetric x-ray heating of exposed materials, to levels as high as  $10^3$ – $10^6$  K, is known to occur under intense XFEL irradiation.<sup>6,9,10</sup> Irradiated samples will exhibit thermal gradients due to beam intensity profiles, inhomogeneous sample absorption, and transport processes. These gradients can then affect probed conditions, particularly where the spatial extent of the thermal gradient is comparable to that of the probing radiation, including in single pulse,<sup>6</sup> pump-probe,<sup>7,11</sup> and pulse train<sup>1,2,4</sup> measurements. While averaging schemes to address the effects of temperature gradients exist,<sup>4,6</sup> their viability is poorly tested particularly where nonlinear behavior, such as phase transformations, may occur.

Here, we discuss the role of thermal gradients in an XFEL experiment using a MHz x-ray pulse repetition rate and time-resolved X-ray diffraction (XRD) measurements. Previous studies have shown that samples under such high-rate x-ray exposure exhibit cumulative heating<sup>1,2,4</sup> broadly consistent with the predictions of numerical models<sup>9</sup> [e.g., Fig. 1(b)]. We further explore the relationship between the states observed within heated samples and the underlying temperature distribution using the phenomenology of a phase transformation occurring under known conditions. Benefits and limitations of using x-ray self-heating measurements, i.e., with x-ray heating of and probing of samples concomitantly, are discussed.

Titanium was chosen as a test subject as it has a known phase transition at moderate temperatures. Under ambient conditions, Ti exhibits a hexagonal-close-packed crystal structure, known as the  $\alpha$ -Ti phase, and undergoes a high temperature phase transition to body-centered-cubic  $\beta$ -Ti at  $T_{\alpha\rightarrow\beta} = 1143$  K.<sup>12</sup>

In this study, we performed time-resolved XRD of MHz-pulsed x-ray heated free-standing Ti. The dynamics and timescale at which the  $\beta$  phase is formed under heating are determined. Under constant (in this case, zero) pressure, we expect that continuous heating of the sample beyond the transition temperature should prompt a transformation to the high-temperature phase. However, a more complex behavior is observed. Numerical

models are employed to investigate the heating and cooling dynamics of pulsed x-ray heating and the effects of spatial temperature gradients on apparent temperature, as probed by XRD. The data presented here were collected as part of a community proposal performed at the European XFEL.<sup>13</sup>

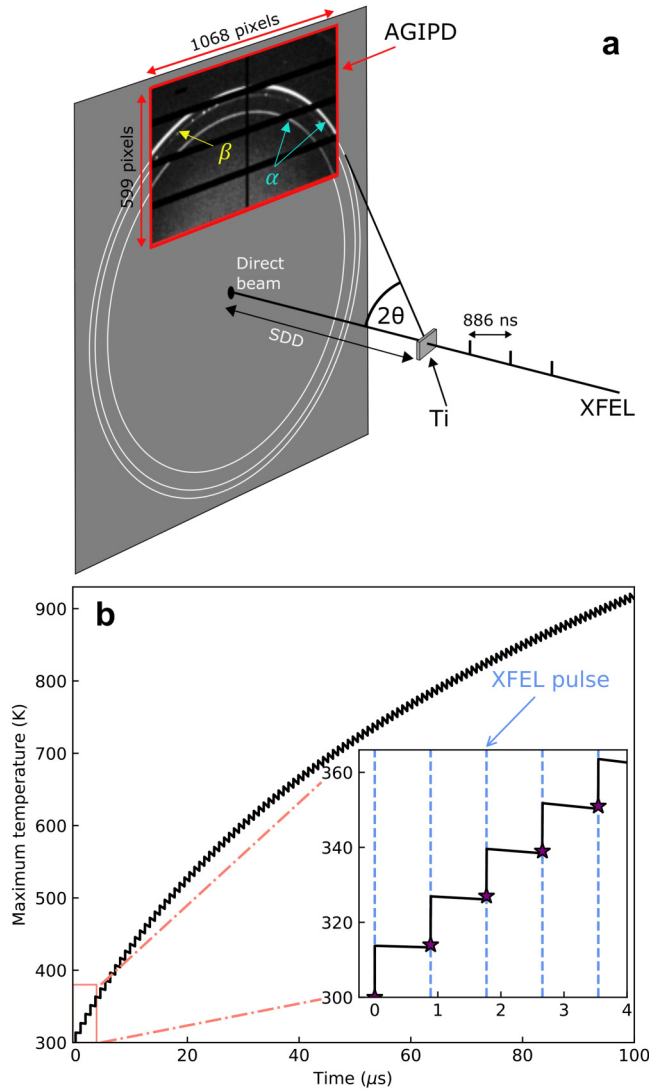
**II. SAMPLE PREPARATION AND METHODOLOGY**

The experiment was performed in interaction chamber 2 (IC2) at the HED instrument, which is located at the end of the SASE2 branch of the European XFEL, Germany.<sup>1,2,14–17</sup> Figure 1(a) shows a simplified schematic of the setup used in this experiment. Each x-ray pulse train consists of 216 pulses at a 1.13 MHz repetition rate with individual x-ray pulse lengths of tens of femtoseconds and 886 ns between each pulse. The x-ray energy was measured to be 18.105 keV with a wavelength of 0.685 Å. The intensity of pulses varies within each train and from train to train. An energy monitor (XGM) upstream of the experimental chamber is used to establish the relative energy on target per pulse.<sup>1,2,18</sup> An XFEL focal spot size of 50  $\mu\text{m}$  full-width half maximum (FWHM) was determined from round-edge scans of the XFEL beam spot.<sup>1</sup>

A single piece of ultra-pure 5  $\mu\text{m}$  thick Ti foil (Goodfellow) was mounted inside IC2. IC2 was kept under vacuum throughout each exposure to a pulse train and samples were taken to remain at zero pressure (transient isochoric pressure perturbations are ignored). Figure 1(b) shows the predicted temperature history of the Ti foil under x-ray heating assuming constant x-ray pulse energy throughout the pulse train. In this study, two heating runs are discussed, at user-selected beam transmissions of 1% and 10% of maximum power, set by trial and error in order to resolve phase transitions within our experimental timeframe.

An Adaptive Gain Integrating Pixel Detector (AGIPD) “mini-half” 500 k,<sup>19</sup> located outside of IC2 behind an Al window,<sup>2</sup> was used to collect angle-dispersive XRD, with a  $2\theta$  Bragg angular coverage between  $7^\circ$  and  $24^\circ$ . The area covered by AGIPD is shown in Fig. 1(a). The AGIPD is capable of collecting diffraction data up to 4.5 MHz and was used at 1.1 MHz here, allowing for pulse-resolved XRD measurements, using a sample-detector

19 September 2024 13:20:56



**FIG. 1.** Experimental setup and predicted temperature of a Ti foil. (a) Experimental setup. The full detection area of the AGIPD is shown with a representative pattern, with the Debye–Scherrer rings of the  $\alpha$  and  $\beta$  phases labeled. (b) FEA modeled peak sample temperature of a Ti foil under irradiation by 112 XFEL pulses at 1.1 MHz assuming a constant energy of  $1\ \mu\text{J}$  per pulse on target. The inset shows the temperature response for the first five pulses. The vertical dashed lines indicate the timings of the XFEL pulses with the peak temperature in the sample probed by the XFEL pulses indicated with stars.

distance of 482.83 mm and the XRD pattern from a  $\text{LaB}_6$  standard as the calibration.

Azimuthal integration of the XRD data yields a 1D pattern of the intensity as a function of  $2\theta$ .<sup>20</sup> The intensity,  $2\theta$  position, and width of each diffraction peak were determined through a least-squares fit of a Gaussian model. The unit-cell volume for the  $\alpha$ -Ti phase was determined from the most intense peaks visible

within the range of the AGIPD [(01 $\bar{1}$ 0), (0002), (10 $\bar{1}$ 1)]. The (0002) peak was not used if it overlapped with the  $\beta$ -Ti (110) peak on the 1D pattern. The  $\beta$ -Ti unit-cell volume was calculated using the position of the (110) reflection. Due to temperature gradients, a unit-cell volume that is measured represents the average over the probed volume of each phase. Temperature is determined from the unit cell volume and the thermal expansion equation of state (EoS) for each phase, with a random error in temperature of  $\sim 25$  K, assessed from the fitting precision.

Finite element analysis (FEA) was performed in cylindrical symmetry about the beam in a constant geometry, including conductive and radiative heat transfer,<sup>1,4,9</sup> although the former (conduction through the foil) dominates. The  $5\ \mu\text{m}$  thick Ti foil is wide enough in the model ( $300\ \mu\text{m}$  radius) to eliminate any edge effects and is surrounded on both sides by vacuum. With an absorption length of  $105\ \mu\text{m}$ <sup>21</sup> (absorption coefficient of  $9524\ \text{m}^{-1}$ ), energy is effectively deposited homogeneously as a function of depth in the foil, and temperature gradients occur only in the lateral (radial) direction due to beam intensity variance and heat conduction over time. We use a density of  $4.5\ \text{g/cc}$ , assumed constant in the model given that deviations from this value with temperature<sup>22,23</sup> have a negligible impact on simulations. For the heat capacity at constant pressure, we use the NIST three-part Shomate model for solid Ti,<sup>24,25</sup> i.e., in  $\alpha$ -Ti separate models for  $300 < T < 700\ \text{K}$  and  $700\ \text{K} < T < T_{\alpha\rightarrow\beta}$  and in  $\beta$ -Ti the model for  $T > T_{\alpha\rightarrow\beta}$  (also used in the case of melting); we note that the models were broadly similar if constant heat capacity (the ambient value of  $525\ \text{J/kg K}$ ) was used instead. Thermal conductivity is taken as  $20\ \text{W/mK}$ , which represents a suitable average over high temperature values.<sup>26</sup> The beam fluence on target delivered per pulse is assessed from the upstream XGM energy monitors, a Gaussian beam profile on target,<sup>9</sup> and the beamline transmission (typically  $\sim 20\%$ – $30\%$  estimated in contemporaneous experiments<sup>1,4</sup>). The beam diameter was initially taken to be  $50\ \mu\text{m}$  FWHM, as measured. The diameter and beamline transmission were varied to improve model agreement with the data in the 10% run. Two models are presented here that match the data satisfactorily well, with a  $50\ \mu\text{m}$  FWHM spot and 19% beamline transmission for a train average of 2.2 and  $20\ \mu\text{J/pulse}$  on target (for 1% and 10% attenuation experiments, respectively); and a somewhat better optimized model, with a  $75\ \mu\text{m}$  FWHM spot, 35% transmission, and 3.9 and  $36\ \mu\text{J/pulse}$ .

In order to compare the FEA model with the data, the apparent temperature that x rays would probe at each time,  $T_{\text{avg}}$ , was computed from a beam-intensity weighted average over the sample temperature gradient,  $T(r, z)$ , as<sup>4</sup>

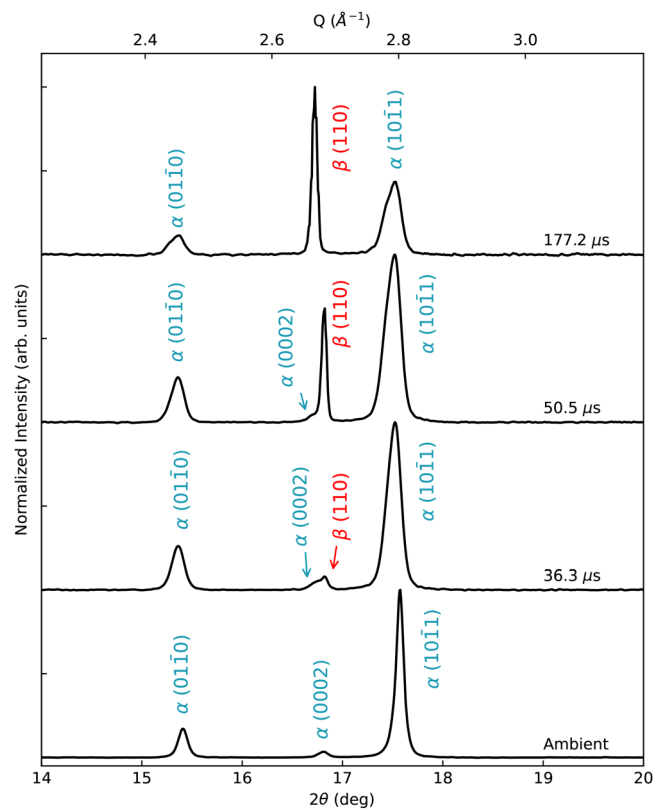
$$T_{\text{avg}} = \frac{1}{N} \int_V 2\pi r T(r, z) \exp\left(-\frac{r^2}{2\sigma_G^2}\right) dz dr, \quad (1)$$

where  $\sigma_G$  is the Gaussian width parameter of the beam<sup>9</sup> and the volume integrated  $V$  is that probed by the x rays in a given measurement. Here, this volume is that of a given phase or structure that gives rise to a particular diffraction signature, which is used to infer the unit cell volume, thermal expansion, and temperature experimentally. For a single-phase material, the volume is just the

19 September 2024 13:20:56

sample volume. For a multiphase system, the volume is restricted to the region of stability of the given phase; this is defined by the range of temperature at which that phase is stable. Hence, the apparent temperature can become multivalued as different phases naturally appear in different temperature domains and, hence, exhibit different average temperatures. The normalization factor  $1/N$  is determined computationally from a reference integration over identical volumes at a fixed temperature.

We further compared the FEA calculation with the experimental data through a forward computation of the diffraction pattern based on the sample temperature gradient from the FEA model. In the simulated XRD, we included relevant effects modifying the diffraction intensity, including the Debye–Waller factor (which reduces the diffraction intensity at higher temperatures), local thermal strain (which affects density and, hence, attenuation), attenuation differences depending on the diffraction angle and position in the sample, the spatial distribution of the x-ray probe, and appropriate mass weighting of the probed volume. Incident fluences were low compared to the saturation regime;<sup>8,27</sup> therefore, electronic excitation was not considered.



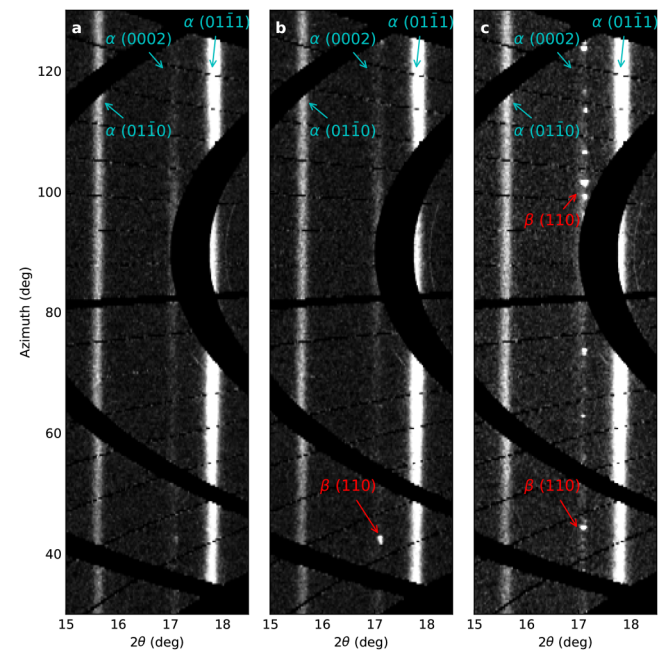
**FIG. 2.** Integrated x-ray diffraction patterns collected from pulses 1, 42, 58, and 201 (or at time 0, 36.3, 50.5, and 177.2  $\mu\text{s}$ ) are shown for the 10% power dataset. Observed reflections from the  $\alpha$ -Ti and  $\beta$ -Ti phases are labeled. The normalized intensity (y axis) of subsequent patterns is shifted for better visibility.

### III. RESULTS

#### A. X-ray diffraction

Under x-ray irradiation, the first pulse in the pulse train probes the ambient sample at room temperature. From the peak positions of the (01 $\bar{1}$ 0), (0002), and (10 $\bar{1}$ 1) reflections of the  $\alpha$  phase, the unit-cell volume is determined. The ambient volume of the  $\alpha$  phase in the 1% run is 35.30  $\text{\AA}^3$ . During heating, the unit-cell volume expands to 35.43  $\text{\AA}^3$  after 120 pulses, or 106.6  $\mu\text{s}$ , but does not increase further after this point (see Sec. III B for details).

When the XFEL beam transmission is increased to 10%, the Ti foil undergoes a phase transformation to the high-temperature  $\beta$  phase. Figure 2 shows the ambient XRD pattern with the three distinct peaks of the  $\alpha$ -Ti phase. The ambient unit cell volume is determined to be 35.28  $\text{\AA}^3$ . The first appearance of the (110) peak of the  $\beta$  phase emerges after 36.3  $\mu\text{s}$  (or 42 pulses) and overlaps with the (0002) peak from the initial  $\alpha$  phase. For all three reflections of the  $\alpha$  phase, the Debye–Scherrer rings showed good powder statistics, i.e., homogenous rings, whereas the (110) reflection of the  $\beta$  phase showed more spotty rings suggesting larger crystallites in the high temperature phase (Fig. 3). As the Ti sample was further heated with time, the amplitude of the (110) reflection of the  $\beta$  phase grew, dwarfing the (0002) reflection of the  $\alpha$  phase. The spotty texture of the (110)  $\beta$  reflection compared to the powder-like texture of the (0002)  $\alpha$  peak allowed for a clear distinction between the two overlapping peaks, as shown in Fig. 3. After 50.5  $\mu\text{s}$  (or 63 XFEL pulses), the (0002) peak of the  $\alpha$  phase is completely indistinguishable from



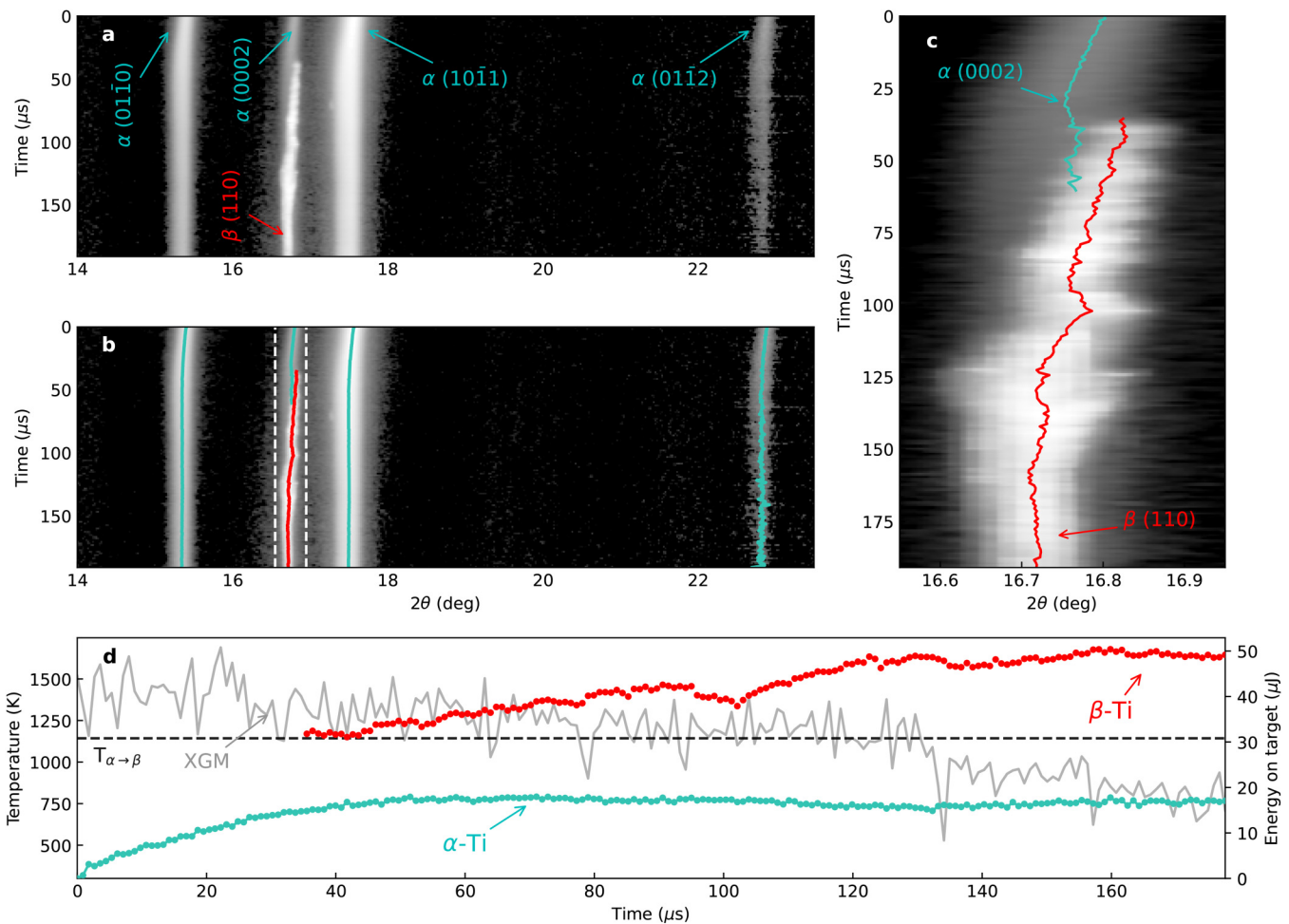
**FIG. 3.** Two-dimensional x-ray diffraction patterns in  $2\theta$  vs azimuthal angle space, collected from pulses 41 (a), 42 (b), and 58 (c) (or at time 35.4, 36.3, and 50.5  $\mu\text{s}$ ) in the 10% power dataset. Observed reflections from the  $\alpha$ -Ti and  $\beta$ -Ti phases are labeled.

19 September 2024 13:20:56

the (110) reflection of the  $\beta$  phase in the 1D pattern. The sudden appearance of the (110) reflection of the  $\beta$  phase in pulse 42 indicates that between XFEL pulse 41 and 42, a sufficient volume of Ti has transformed for the detection of the  $\beta$  phase with XRD.

Figures 4(a) and 4(b) show the XRD from the full heating cycle of the Ti foil at 10% transmission. A close-up of the (110) reflection from the  $\beta$  phase is shown in Fig. 4(c). After formation of the  $\beta$  phase, the (110) reflection rapidly increases in amplitude while also shifting to a lower two-theta value with time, indicating a volume expansion. At the same time, volume expansion of the alpha phase ceased.

The temperature is determined from the measured volume of the  $\alpha$  and  $\beta$  phases of Ti and their known volumetric thermal expansion [Fig. 4(d)]. We use the thermal EoS of  $\alpha$ -Ti described by Zhang *et al.*<sup>28</sup> and a constant thermal expansion of the  $\beta$ -Ti phase as given by Senkov *et al.*<sup>23</sup> For the 1% transmission run, the thermal expansion of the volume of the  $\alpha$  phase suggests that the sample temperature reaches a maximum of about 456 K (Sec. III B). For the 10% transmission run, the  $\alpha$  phase reaches a maximum temperature of 755 K with a measured volume of 35.70  $\text{\AA}^3$  and the  $\beta$  phase has a maximum temperature of 1679 K with a measured volume of 37.02  $\text{\AA}^3$ . When the  $\beta$  phase is first observed, at 36.3  $\mu\text{s}$ ,



19 September 2024 13:20:56

**FIG. 4.** X-ray heating and diffraction data of a free-standing Ti foil, with an x-ray beam transmission set to 10%. (a) Azimuthally integrated XRD data as a function of time (or pulse). The reflections from the  $\alpha$ -Ti and  $\beta$ -Ti phases are shown in blue and red, respectively. (b) Same as (a) but with fitted peak positions overlaid. The dashed lines show the  $2\theta$  range shown in (c). Fluctuations in the XFEL pulse energy in a single pulse train, are accounted for by normalization of the peak intensity by employing photodiode records, which were absolutely calibrated against XGM values.<sup>18</sup> (c) Close-up of the  $\beta$ -Ti phase, with the measured position of the (110) reflection shown in red. The position of the (0002) reflection of the  $\alpha$ -Ti phase is shown in blue. (d) Calculated temperature of the  $\alpha$ -Ti and  $\beta$ -Ti phases. The measured energy on target (XGM) is shown for reference, calculated from the SASE2 XGM<sup>18</sup> multiplied by a baseline beamline transmission of 30% and the user selected transmission (10%). The dashed line indicates 1143 K, the reported temperature of the  $\alpha$ - $\beta$  transition in Ti.

the temperature of the  $\beta$  phase is 1170 K, whereas the temperature of the  $\alpha$  phase, at this time, is 714 K.

The above temperatures represent the averages over the temperature distribution in each phase. This distribution was examined by considering changes in the peak width, i.e., thermal broadening. Peak broadening due to temperature was analyzed for the case of the  $\alpha$ -Ti ( $10\bar{1}1$ ) and ( $01\bar{1}0$ ) peaks at 10% XFEL power since the signal is strong enough to resolve the peak shape precisely and the data exhibit good powder diffraction. The thermal gradient in the sample was estimated from the symmetric broadening of the fitted peak width, assuming a linear addition of the thermal broadening component ( $FWHM_{th}$ ) and initial (instrumental) width ( $FWHM_i$ ). Each reflection is treated independently to one another. The maximum and minimum temperature then probed by the XFEL beam can be determined from the maximum and minimum volume, respectively, estimated using  $2\theta$  central peak positions and downshifting and upshifting, respectively, by  $FWHM_{th}/2$ . Figure 5(a) shows how the measured FWHM of the ( $10\bar{1}1$ ) and ( $01\bar{1}0$ ) peaks increases as the Ti foil is heated, as a result of thermal broadening. The maximum and minimum temperature of the  $\alpha$  phase indicated by the broadening is plotted in Fig. 5(b).

When  $\beta$ -Ti appears in the XRD, the temperature range in the probed  $\alpha$ -Ti phase should reach its maximum (i.e., 300 K for the unheated portion of the sample, close to the beam edges, and 1143 K for the hottest part of the sample, close to the  $\alpha$ - $\beta$  transition temperature). As expected, this time correlates with the detected temperature range also reaching a maximum value. Furthermore, the maximum and minimum temperatures detected at later times in  $\alpha$ -Ti remain in close agreement with the  $\alpha$ - $\beta$  phase transition temperature and room temperature, respectively.

Thermal broadening for the spotty  $\beta$ -Ti peaks was also measured; however, a much smaller range of temperatures than the  $\alpha$  phase was observed [Fig. 5(b)]. Minimal or no broadening in the peak shape was found for the first  $25\ \mu\text{s}$  after the  $\beta$  phase was formed, suggesting that initially, we are observing individual crystallites of  $\beta$ -Ti at a constant temperature.

Thus, the peak shape data can directly determine the temperature range of heated phases, including the phase transition temperature, with a precision of order  $\sim 100$  K in this case, even using a first-order approximation of symmetric, Gaussian-like broadening, and considering other requirements, such as an ideal powder signal.

## B. Numerical modeling

Figure 6 shows results from finite modeling analysis of serial heating of the Ti foil at 1% and 10% XFEL beam transmission, compared with XRD data. As previously introduced, the temperature response of the foil under irradiation was calculated using two different XFEL beam FWHM ( $50$  and  $75\ \mu\text{m}$ ), and the parameters for each were set primarily to match the 10% data. Specifically, the aim was to optimize the match of simulated  $T_{avg}$  to best reproduce the XRD-determined temperature evolution for both the  $\alpha$ -Ti and  $\beta$ -Ti phases.

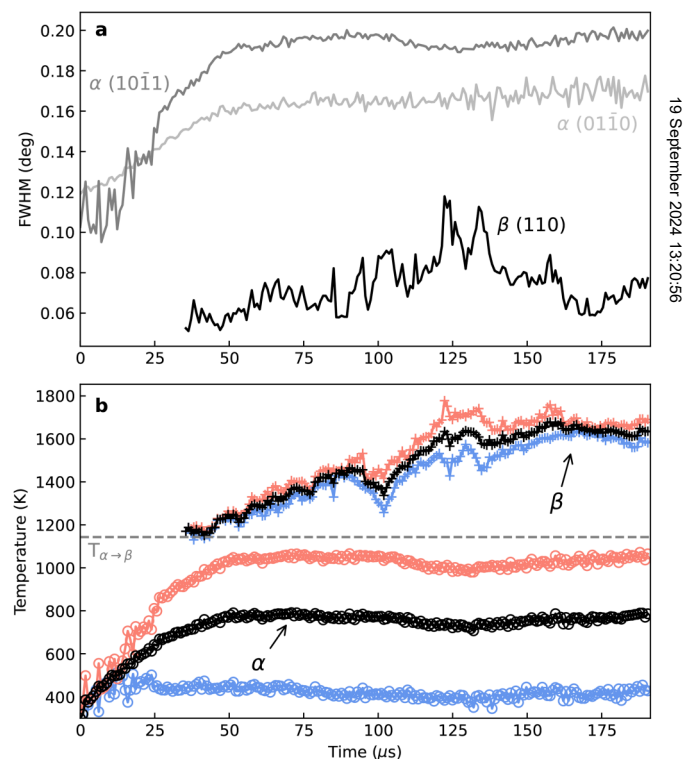
In both experimental runs, the temperature of the  $\alpha$  phase is observed to first increase with time as more XFEL pulses have been incident on the sample and then reach relatively constant values at later times. In the case of the 1% data, FEA predicts that this effect

results from the gradual approach to an equilibrium between pulse heating and inter-pulse cooling,<sup>9</sup> combined with some decrease in pulse energy over the train [Fig. 4(d)]; no sharp changes are seen. In the case of the 10% data, there is a sharp kink in the temperature trend predicted for  $\alpha$ -Ti, and a plateau at later times, associated with the onset of the solid–solid phase transition.

During the run at 10%, the  $\beta$  phase will start to form when the maximum temperature ( $T_{max}$ ) within the foil, i.e., at the center of the Gaussian beam profile, crosses the high-temperature phase boundary. As the sample is further heated, the volume of material transformed into the  $\beta$  phase grows, while its average and maximum temperature increase.

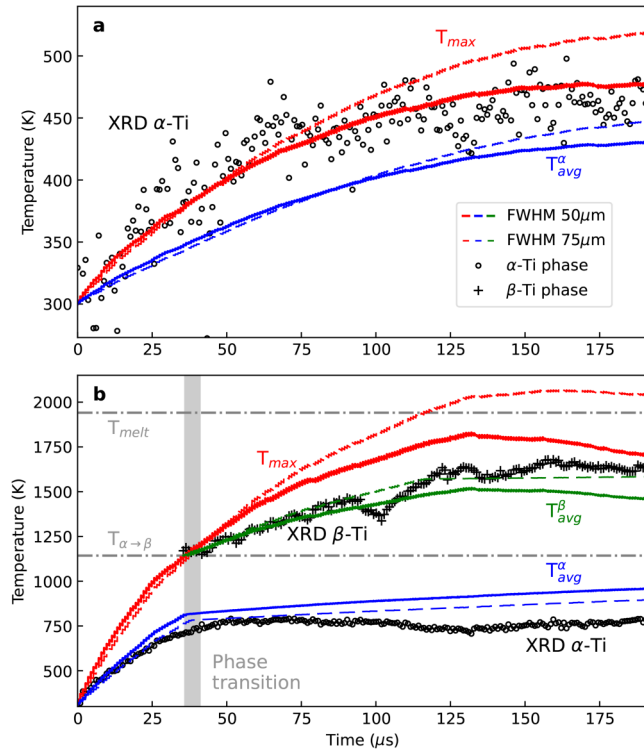
In the  $50\ \mu\text{m}$  diameter beamspot simulation, the model indicates that the sample does not melt during the experiments. However, with the larger beamspot, the melting point is just reached after  $\sim 120\ \mu\text{s}$  ( $T_{max} > 1941$  K), manifesting itself as a secondary plateau in the model, now in the  $\beta$  phase, due to a second phase transformation to liquid.

The larger diameter beamspot simulation is considered to match the data somewhat better. The agreement of  $T_{avg}$  with the experimental plateau in the  $\alpha$ -Ti temperature after  $\sim 36\ \mu\text{s}$  is closer,



**FIG. 5.** Thermal broadening of the  $\alpha$  and  $\beta$  phases. (a) Fitted peak FWHM of the ( $01\bar{1}0$ ) and ( $10\bar{1}1$ ) peaks of  $\alpha$ -Ti and the ( $110$ ) peak of  $\beta$ -Ti. (b) Temperature of the  $\alpha$ -Ti and  $\beta$ -Ti phase from the fitted peak position (black), with temperature maximum and minimum inferred from peak broadening given in red and blue, respectively.

19 September 2024 13:20:56

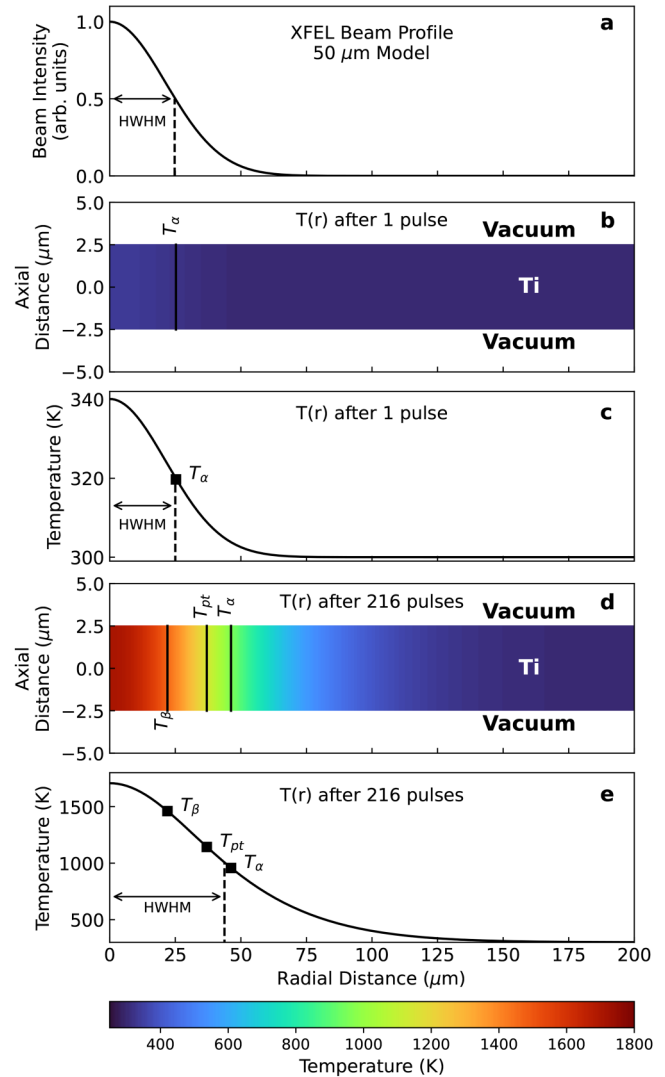


**FIG. 6.** XRD and FEA temperature of a Ti foil during irradiation with 216 XFEL pulses at 1% (a) and 10% (b) XFEL beam transmission. The maximum temperature ( $T_{max}$ ) and the average temperature of the  $\alpha$  ( $T_{avg}^{\alpha}$ ) and  $\beta$  ( $T_{avg}^{\beta}$ ) phases are shown as red, blue, and green lines, respectively. The FWHM of the XFEL beam used in the FEA models shown here was  $50\mu\text{m}$  (solid lines) and  $75\mu\text{m}$  (dashed lines). The XRD-determined temperature of the  $\alpha$  (open circles) and  $\beta$  (crosses) phases is shown.

and this model produces a plateau also in the  $\beta$  phase, which matches an apparent plateau or limit in the  $\beta$ -Ti temperature after  $120\mu\text{s}$ . However, the general features of the model are similar in both simulations.

The FWHM of the radial temperature distribution in the foil after a single XFEL pulse is comparable to the FWHM of the XFEL beam profile, i.e., in the smaller diameter, 10% simulation, the FWHM of the beamspot and the thermal gradient is  $50.0\mu\text{m}$ , and both are Gaussian in shape (Fig. 7). However, after 216 pulses, the radial temperature distribution in the foil exhibits an  $87.5\mu\text{m}$  FWHM, significantly broader than that of the beam profile, although it maintains a Gaussian shape. The radial broadening is due to conduction outward into the bulk Ti with time and leads to reduced local temperature gradients.

The directly calculated diffraction pattern on the basis of the FEA modeled temperature gradient (Fig. 8) is normalized to match the most intense  $\alpha$ -Ti peak. The data show generally good agreement of peak intensities for  $\alpha$ -Ti, with some initial texture in the foil indicated by a minor peak amplitude mismatch. The apparent temperature from fitting the model peaks ( $995.0\text{K}$  at the time of the

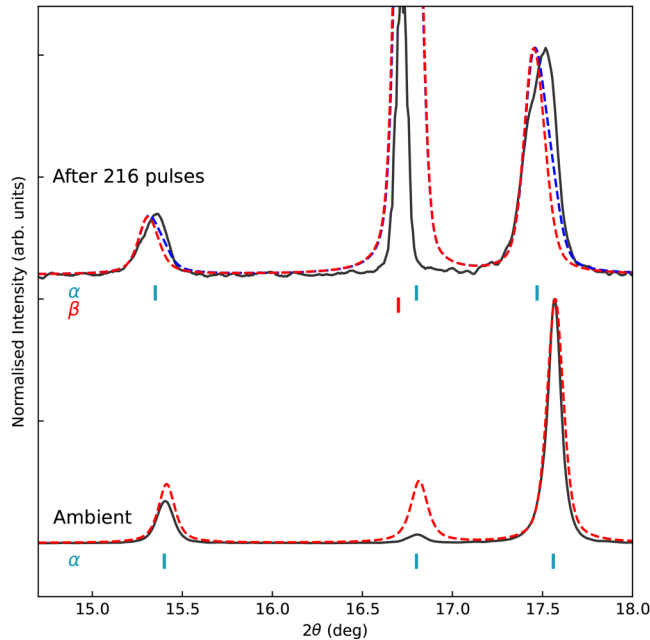


**FIG. 7.** Results of FEA for  $5\mu\text{m}$  of a Ti foil under irradiation by 216 XFEL pulses at 10% power. (a) XFEL beam profile as a function of the radial distance from the center of the beam. The FWHM of the XFEL beam is  $50\mu\text{m}$ . (b) Axial and radial temperature distribution after a single XFEL pulse ( $1 \times 10^{-8}\text{s}$  after initial x-ray exposure). (c) The radial temperature gradient after a single XFEL pulse. The FWHM of the temperature gradient in the radial direction is  $50\mu\text{m}$ . (d) Axial and radial temperature distribution after 216 pulses ( $1.9 \times 10^{-4}\text{s}$  after initial x-ray exposure). (e) The radial temperature gradient after 216 pulses. The FWHM of the temperature gradient in the radial direction is  $87.5\mu\text{m}$ . There is no temperature gradient in the axial direction. The radial position at which the temperature in the foil is equal to the average temperature of the  $\alpha$  and  $\beta$  phases is marked as  $T_{\alpha}$  and  $T_{\beta}$ , respectively.  $T_{pt}$  indicates the radial position where the temperature inside the foil is equal to the temperature of the phase transition between the  $\alpha$  and  $\beta$  phases.

last XFEL pulse) is in good agreement with the average [Eq. (1)] model temperatures ( $989.5\text{K}$  at the same time), showing the complementarity of these two approaches for representing the apparent temperature, at least where good averaging over continuous

19 September 2024 13:20:56





**FIG. 8.** Simulated XRD pattern (red dashed) of a Ti sample at ambient conditions, and after irradiation by 216 XFEL pulses, for the  $50\text{ }\mu\text{m}$  FWHM beamspot simulation. The measured integrated XRD pattern is shown in black. Also shown is a simulation, including a beam tail (blue dashed), comprising 99% intensity from the  $50\text{ }\mu\text{m}$  diameter beamspot and 1% intensity from a  $150\text{ }\mu\text{m}$  diameter beamspot.

temperature distributions can be assumed. The agreement becomes somewhat poorer as beta-Ti is formed, with sharper peaks in the experiment than in the simulation, which will be discussed below.

#### IV. DISCUSSION

Our findings explore the potentially complex relationship between the apparent temperatures measured in heated samples and the temperature distributions within the probed area for the common case of self-heating of targets during probing by x-ray free electron laser radiation. Radial beam intensity gradients, continuous pulsed heating, and thermal conduction within samples all contribute to the temperature variation and measured values.

In the present example, individual temperature excursions during heating events are small [Figs. 1(b) and 6] compared to the overall rise in temperature. This occurs because the beam profile is large in size compared to the characteristic heat diffusion distance<sup>9</sup> between heating events,  $d \sim \sqrt{\kappa/R}$ , where  $\kappa$  is the thermal diffusivity ( $\sim 8.4\text{ mm}^2/\text{s}$  for Ti) and  $R$  is the repetition rate (1.13 MHz), or  $d \sim 3\text{ }\mu\text{m}$ . Simulations with beam focal sizes comparable to  $d$  generate significantly greater transient temperature variations. The high thermal inertia of the freestanding foil, compared with a system undergoing rapid cooling into surrounding materials,<sup>9</sup> also contributes to the relatively gradual heating. In this case, the shape of the temperature distribution evolves slowly (Fig. 7) and

exclusively due to lateral heat diffusion in the foils due to insignificant radiative losses.

During heating to high temperature, at  $\sim 36\text{ }\mu\text{s}$  where the phase transition initiates, the bulk of the probed volume remained in the  $\alpha$  phase with an average temperature of  $\sim 700\text{ K}$ . The thermal EoS of the  $\beta$  phase gives a temperature of  $1150\text{--}1170\text{ K}$  at similar times (Fig. 4). This suggests that as the peak temperature of the hot spot crosses the high-temperature phase boundary from the  $\alpha$  to the  $\beta$  phases ( $1143\text{ K}$ ), the material locally transforms while the material toward the edges that is colder stays in the  $\alpha$  phase. At this moment, several temperatures converge, i.e.,  $T_{avg}^{\beta} = T_{max} = T_{\alpha\rightarrow\beta}$ . Only at this specific time is the sample maximum temperature determined directly from diffraction peak position. As further heating occurs, the volume of the  $\beta$  phase grows, and the beam weighted average temperature in this phase diverges from the maximum. Spotty diffraction, from individual  $\beta$  crystallites in the temperature gradient, contributes to some irregular variation in the probed temperatures for this phase, but produces values between  $T_{\alpha\rightarrow\beta}$  and  $T_{max}$ , as expected.

That the apparent temperature of the  $\beta$  phase upon formation can be so much higher than that of the  $\alpha$  phase, rather than showing the  $\alpha$  phase approach the transition temperature, is clarified by examination of the FEA models. For example, when the sample peak temperature reaches  $T_{\alpha\rightarrow\beta}$ , the  $\alpha$  phase volume fraction at  $T_{\alpha\rightarrow\beta}$  is precisely zero (occurring only on the central axis of the beam) and, therefore, cannot be detected in this limit with volumetric probes, such as XRD. However, the distribution of phase temperatures, up to the transition temperature in this case, is still potentially detectable through examination of the diffraction lineshapes.

The biasing of apparent sample temperatures as a result of thermal and beam gradients is observed despite this relatively gradual heating, where the formation of steep gradients by fast cooling<sup>9</sup> is inhibited. Similarly, as time progresses and heat conducts laterally, the temperature gradient of the probed region, within the beam FWHM [Fig. 7(a)], decreases dramatically from 50%–100% of the maximum [Fig. 7(c)] to  $>82\text{--}100\%$  in the case of the smaller diameter beamspot simulation [Fig. 7(e)]. Yet, there is little corresponding reduction of the biasing effects [Fig. 6(b)]. Thus, biasing can be present even in the case of small temperature gradients.

The large thermal gradients within the sample place limitations on the accuracy of phase transition boundary identification, as apparent temperature measurements for a particular phase can sample the bulk average temperature rather than the hottest temperature a phase exists at. Similarly, the emergence of a high-temperature phase can occur only above the phase transition boundary, which can lead to an apparent jump in the temperature between two phases, rather than a continuous temperature evolution, as expected thermodynamically.

This becomes important when XRD measurements are used to establish heating in samples. For example, in Ref. 2, using XFEL probing to study dynamic compression in a diamond anvil cell, a preliminary x-ray exposure prior to dynamic compression is conducted to assess the magnitude of x-ray heating. In such an experiment, the existence of thermal gradients within the sample would lead to a broadening of XRD peaks as a result of probing a

distribution of temperatures and an underestimation of the peak sample temperature from peak positions alone. This could in turn influence assessed pressures during dynamic compression; for example, if phase transformation pressure varied with temperature, the pressure of the first appearance of a phase will correspond to either the minimum or maximum sample temperature, not the average temperature, and, therefore, depends on the Clapeyron slope of the phase transformation and the full temperature range in the sample. This effect can be characterized through analysis of the peak shape and numerical modeling.

While some sluggish phase transitions are known for Ti,<sup>29</sup> we do not believe this plays any role in our measurements as we observe the high-temperature  $\beta$  phase transition at the expected temperature.<sup>30</sup> Similarly, timescales are long compared to lattice thermalization timescales. Thus, equilibrium thermal and thermodynamic conditions are probed in these experiments.

While initial numerical models adequately described the observed thermal response of the samples, the adjustment of model beam properties, such as focal spot FWHM, improved the quantitative match to the observed temperature evolution. In particular, a beam broader than the one measured experimentally predicted a larger gap between the observed temperatures of the  $\alpha$  and  $\beta$  phases, which is more consistent with the observations. This discrepancy is likely due to the model assuming a perfect Gaussian profile. In contrast, the true beam profile is closer to that of a double Gaussian, with a significantly larger tail.<sup>1,31</sup> As temperature determinations from XRD probe the average temperature, the larger beam tails can reduce the apparent temperature as more cold material would be included in the average, which is approximately modeled here using a broader Gaussian beam profile. Other factors could also bias the measurement to colder temperatures, such as the Debye–Waller effect.

When forward modeling the x-ray diffraction data from FEA models (Fig. 8), accounting for details such as the local probe intensity, the Debye–Waller factor, and temperature-dependent x-ray attenuation, we observe reasonable agreement with the experimentally measured diffraction patterns both for the initial (cold) pattern and the final (heated) pattern. This is particularly true for the  $\alpha$ -Ti phase where the peak shift and broadening are comparable between the simulated and measured patterns. However, the simulated pattern exhibits a moderately larger peak shift, consistent with the average of the simulated temperature distribution [Eq. (1)] also implying a higher apparent temperature than observed [Fig. 6(b)]. Improvements in the agreement between simulation and experiment, i.e., a reduced peak shift and broader peaks, can be achieved by broadening the sampling of the temperature distribution used to model the diffraction, for example, by including a tail on the beam profile, thereby adding more cold material to the average (Fig. 8). In the case of the  $\beta$ -Ti phase, more significant differences between simulation and experiment are encountered. Although the simulated peak shift in this phase is smaller than the experimental shift, again consistent with weighted average findings [Fig. 6(b)], the experimental peak is also much sharper, and weaker than expected, which we attribute to the spotty  $\beta$ -Ti patterns (Fig. 3). The texture and poor grain statistics in the  $\beta$  phase limit the diffraction sampling of the temperature gradient, and given that models assume proportionate sampling of the computed continuous gradient, this

leads to a poorer comparison between the data and models. In fact, the FEA model generally predicts a larger domain of  $\beta$ -Ti with time and an increase in the temperature range between the peak sample temperature and that of the  $\alpha$ - $\beta$  phase transformation. This is not observed in our experiment, in which the temperature gradients probed by x-ray diffraction in  $\beta$ -Ti are small at all times (Fig. 5). This may be due to the presence of smaller grains with weaker scattering power under certain conditions.

The model also assumes a stably aligned and focused train of pulses arriving at the sample. Other experiments have shown that the beam pointing and the focal shape during the pulse train are generally reproducible<sup>31</sup> such that the beam position instability cannot explain the general behavior of the features observed in the diffraction. However, some amount of drift in the position or shape could contribute to the detailed characteristics of the data, such as including more colder material in the diffraction averaging. Finally, the  $\alpha$  phase temperature does not simply stop increasing during heating, and then increase sluggishly, as modeled; rather, it decreases somewhat (Fig. 6), producing a dip later in the record (near 130  $\mu$ s). Remarkably, the dip is directly correlated with the maximum modeled sample temperature. This feature may also be related to the adequacy of our beam or averaging model or other effects, such as thermal stress in the sample.

## V. CONCLUSION

We have examined how, under irradiation by a series of XFEL pulses, a titanium sample undergoes serial volumetric heating. The apparent temperature evolution of the sample—based on x-ray diffraction measurements from this same pulse train—is compared to numerical models, giving insight into the temperature dynamics within the sample and effects of large temperature gradients on apparent temperature. Good agreement is found between the XRD-determined and model-predicted temperature evolution.

We observe in Ti the emergence of the high-temperature  $\beta$  phase at a completely different apparent temperature to the low-temperature  $\alpha$  phase. The prominent radial temperature gradient within the foil gives rise to the large apparent temperature difference between the two phases. That is, the first-order temperature-driven phase transition exhibits discontinuous behavior in apparent temperatures despite the presence of a continuous temperature distribution, with limiting temperatures of the low-temperature phase well below the known transition temperature. This is even the case after heat conduction has reduced temperature gradients in the probed region to relatively small values. Hence, treating observed conditions as simple averages over irradiated samples is not effective where rapid, nonlinear changes in state, such as phase transformation, occur, as these need to be accounted for explicitly in averaging schemes along with the impact on specific measurements.

Our findings support future experimental measurements for more complex and unknown systems, particularly where accurate temperature assessment is critical to establishing the conditions explored using XFEL irradiation.

## ACKNOWLEDGMENTS

We acknowledge European XFEL in Schenefeld, Germany, for provision of x-ray free-electron laser beamtime at Scientific

Instrument HED (High Energy Density Science) and would like to thank the staff for their assistance. The authors are indebted to the HIBEF user consortium for the provision of instrumentation and staff that enabled this experiment. O.B.B. acknowledges the support of the Scottish Doctoral Training Program in Condensed Matter Physics (CM-CDT). J.D.M. acknowledges support from EPSRC and AWE CASE studentships, UK Ministry of Defence © Crown Owned Copyright 2022/AWE. This research was supported through the European Union's Horizon 2020 Research and Innovation Program (ERC Grant Nos. 864877 and 101002868). UK Research and Innovation (UKRI) support is acknowledged from the EPSRC Grant EP/R02927X/1 (MIM) and the Science and Technology Facilities Council (STFC) grant ST/V000527/1 (EK). Z.K. and C.P. acknowledge support from the DFG (Project No. KO-5262/1). A.F.G. acknowledges the National Science Foundation (Grant No. DMR-2200670) and the Carnegie Science support. V.B.P. acknowledges the National Science Foundation—Earth Sciences (EAR—1634415). C.-S.Y. acknowledges the funding of DOE-NNSA (No. DE-NA-0004091) and NSF (No. DMR 2112653), supporting the effort at WSU. G.M. has been supported by a grant from Labex OSUG@2020 (Investissements d'avenir—ANR10 LABX56), as well as from the Programme National de Planetologie (PNP) of CNRS/INSU. This work was performed under the auspices of the U.S. Department of Energy by the Lawrence Livermore National Laboratory under Contract No. DE-AC52-07NA27344. This research was supported by the German Science Foundation DFG through Research Unit FOR 2440/2 “Matter Under Planetary Interior Conditions” (Grant No. SA 2585/5-1). For the purpose of open access, the author has applied a Creative Commons Attribution (CC BY) license to this submission.

## AUTHOR DECLARATIONS

### Conflict of Interest

The authors have no conflicts to disclose.

### Author Contributions

**O. B. Ball:** Formal analysis (equal); Methodology (equal); Writing – original draft (equal); Writing – review & editing (equal). **R. J. Husband:** Data curation (equal); Formal analysis (equal); Writing – original draft (equal); Writing – review & editing (equal). **J. D. McHardy:** Data curation (equal); Formal analysis (equal); Writing – original draft (equal); Writing – review & editing (equal). **M. I. McMahon:** Data curation (equal); Formal analysis (equal); Writing – original draft (equal); Writing – review & editing (equal). **C. Strohm:** Data curation (equal); Formal analysis (equal); Writing – review & editing (equal). **Z. Konôpková:** Data curation (equal); Formal analysis (equal); Writing – review & editing (equal). **K. Appel:** Data curation (equal); Writing – review & editing (equal). **V. Cerantola:** Data curation (equal); Writing – review & editing (equal). **A. L. Coleman:** Data curation (equal); Writing – review & editing (equal). **H. Cynn:** Data curation (equal); Writing – review & editing (equal). **A. Dwivedi:** Data curation (equal); Writing – review & editing (equal). **A. F. Goncharov:** Data curation (equal); Writing – review & editing (equal). **H. Graafsma:** Data curation (equal); Writing – review & editing (equal). **L. Q. Huston:**

Data curation (equal); Writing – review & editing (equal). **H. Hwang:** Data curation (equal); Writing – review & editing (equal). **J. Kaa:** Data curation (equal); Writing – review & editing (equal). **J.-Y. Kim:** Data curation (equal); Writing – review & editing (equal). **E. Koemets:** Data curation (equal); Writing – review & editing (equal). **T. Laurus:** Data curation (equal); Writing – review & editing (equal). **X. Li:** Data curation (equal); Writing – review & editing (equal). **H. Marquardt:** Data curation (equal); Writing – review & editing (equal). **A. S. J. Méndez:** Data curation (equal); Writing – review & editing (equal). **S. Merkel:** Data curation (equal); Writing – review & editing (equal). **A. Mondal:** Data curation (equal); Writing – review & editing (equal). **G. Morard:** Data curation (equal); Writing – review & editing (equal). **V. B. Prakapenka:** Data curation (equal); Writing – review & editing (equal). **C. Prescher:** Data curation (equal); Writing – review & editing (equal). **T. R. Preston:** Data curation (equal); Writing – review & editing (equal). **S. Speziale:** Data curation (equal); Writing – review & editing (equal). **S. Stern:** Data curation (equal); Writing – review & editing (equal). **B. T. Sturtevant:** Data curation (equal); Writing – review & editing (equal). **N. Velisavljevic:** Data curation (equal); Writing – review & editing (equal). **C.-S. Yoo:** Data curation (equal); Writing – review & editing (equal). **U. Zastra:** Data curation (equal); Project administration (equal); Writing – review & editing (equal). **Zs. Jenei:** Data curation (equal); Project administration (equal); Writing – review & editing (equal). **H. P. Liermann:** Data curation (equal); Project administration (equal); Writing – review & editing (equal). **R. S. McWilliams:** Data curation (equal); Formal analysis (equal); Supervision (equal); Writing – original draft (equal); Writing – review & editing (equal).

## DATA AVAILABILITY

The data that support the findings of this study are openly available in the data management portal for European XFEL (myMdc) at <https://in.xfel.eu/metadata/doi/10.22003/XFEL.EU-DATA-002592-00>. Raw data were generated at European XFEL. Derived data supporting the findings of this study are available from the corresponding author upon reasonable request.

## REFERENCES

- <sup>1</sup>H. P. Liermann, Z. Konôpková, K. Appel, C. Prescher, A. Schropp, V. Cerantola, R. J. Husband, J. D. McHardy, M. I. McMahon, R. S. McWilliams, C. M. Pépin, J. Mainberger, M. Roeper, A. Berghäuser, H. Damker, P. Talkovskii, M. Foese, N. Kujala, O. B. Ball, M. A. Baron, R. Briggs, M. Bykov, E. Bykova, J. Chantel, A. L. Coleman, H. Cynn, D. Dattelbaum, L. E. Dresselhaus-Marais, J. H. Eggert, L. Ehm, W. J. Evans, G. Fiquet, M. Frost, K. Glazyrin, A. F. Goncharov, H. Hwang, Z. Jenei, J.-Y. Kim, F. Langenhorst, Y. Lee, M. Makita, H. Marquardt, E. E. McBride, S. Merkel, G. Morard, E. F. O'Bannon, C. Otzen, E. J. Pace, A. Pelka, J. S. Pigott, V. B. Prakapenka, R. Redmer, C. Sanchez-Valle, M. Schoelmerich, S. Speziale, G. Spiekermann, B. T. Sturtevant, S. Toilekiki, N. Velisavljevic, M. Wilke, C.-S. Yoo, C. Baecht, U. Zastra, and C. Strohm, “Novel experimental setup for megahertz X-ray diffraction in a diamond anvil cell at the High Energy Density (HED) instrument of the European X-ray Free-Electron Laser (EuXFEL),” *J. Synchrotron Radiat.* **28**, 688 (2021).
- <sup>2</sup>R. J. Husband, C. Strohm, K. Appel, O. B. Ball, R. Briggs, J. Buchen, V. Cerantola, S. Chariton, A. L. Coleman, H. Cynn, D. Dattelbaum, A. Dwivedi,

- J. H. Eggert, L. Ehm, W. J. Evans, K. Glazyrin, A. F. Goncharov, H. Graafsma, A. Howard, L. Huston, T. M. Hutchinson, H. Hwang, S. Jacob, J. Kaa, J. Kim, M. Kim, E. Koemets, Z. Konôpková, F. Langenhorst, T. Laurus, X. Li, J. Mainberger, H. Marquardt, E. E. McBride, C. McGuire, J. D. McHardy, M. I. McMahon, R. S. McWilliams, A. S. J. Méndez, A. Mondal, G. Morard, E. F. O'Bannon, C. Otzen, C. M. Pépin, V. B. Prakapenka, C. Prescher, T. R. Preston, R. Redmer, M. Roeper, C. Sanchez-Valle, D. Smith, R. F. Smith, D. Sneed, S. Speziale, T. Spitzbart, S. Stern, B. T. Sturtevant, J. Sztuk-Dambietz, P. Talkovski, N. Velisavljevic, C. Vennari, Z. Wu, C.-S. Yoo, U. Zastrau, Z. Jenei, and H.-P. Liermann, "A MHz x-ray diffraction set-up for dynamic compression experiments in the diamond anvil cell," *J. Synchrotron Radiat.* **30**, 671–685 (2023).
- <sup>3</sup>H. Hwang, T. Kim, H. Cynn, T. Vogt, R. J. Husband, K. Appel, C. Baetz, O. B. Ball, M. A. Baron, R. Briggs, M. Bykov, E. Bykova, V. Cerantola, J. Chantel, A. L. Coleman, D. Dattelbaum, L. E. Dresselhaus-Marais, J. H. Eggert, L. Ehm, W. J. Evans, G. Fiquet, M. Frost, K. Glazyrin, A. F. Goncharov, Z. Jenei, J. Kim, Z. Konôpková, J. Mainberger, M. Makita, H. Marquardt, E. E. McBride, J. D. McHardy, S. Merkel, G. Morard, E. F. O'Bannon, C. Otzen, E. J. Pace, A. Pelka, C. M. Pépin, J. S. Pigott, V. B. Prakapenka, C. Prescher, R. Redmer, S. Speziale, G. Spiekermann, C. Strohmann, B. T. Sturtevant, N. Velisavljevic, M. Wilke, C.-S. Yoo, U. Zastrau, H.-P. Liermann, M. I. McMahon, R. S. McWilliams, and Y. Lee, "X-ray free electron laser-induced synthesis of iron nitride at high pressures," *J. Phys. Chem. Lett.* **12**, 3246–3252 (2021).
- <sup>4</sup>O. B. Ball, C. Prescher, K. Appel, C. Baetz, M. A. Baron, R. Briggs, V. Cerantola, J. Chantel, S. Chariton, A. L. Coleman, H. Cynn, H. Damker, D. Dattelbaum, L. E. Dresselhaus-Marais, J. H. Eggert, L. Ehm, W. J. Evans, G. Fiquet, M. Frost, K. Glazyrin, A. F. Goncharov, R. J. Husband, H. Hwang, N. Jaisle, Z. Jenei, J.-Y. Kim, Y. Lee, H. P. Liermann, J. Mainberger, M. Makita, H. Marquardt, E. E. McBride, J. D. McHardy, M. I. McMahon, S. Merkel, G. Morard, E. F. O'Bannon, C. Otzen, E. J. Pace, A. Pelka, C. M. Pépin, J. S. Pigott, C. Plückerthun, V. B. Prakapenka, R. Redmer, S. Speziale, G. Spiekermann, C. Strohmann, B. T. Sturtevant, P. Talkovski, L. Wollenweber, U. Zastrau, R. S. McWilliams, and Z. Konôpková, "Dynamic optical spectroscopy and pyrometry of static targets under optical and x-ray laser heating at the European XFEL," *J. Appl. Phys.* **134**, 055901 (2023).
- <sup>5</sup>E. J. Pace, A. L. Coleman, R. J. Husband, H. Hwang, J. Choi, T. Kim, G. Hwang, S. H. Chun, D. Nam, S. Kim, O. B. Ball, H.-P. Liermann, M. I. McMahon, Y. Lee, and R. S. McWilliams, "Intense reactivity in sulfur-hydrogen mixtures at high pressure under x-ray irradiation," *J. Phys. Chem. Lett.* **11**, 1828–1834 (2020).
- <sup>6</sup>S. M. Vinko, O. Ciricosta, B. I. Cho, K. Engelhorn, H.-K. Chung, C. R. D. Brown, T. Burian, J. Chalupský, R. W. Falcone, C. Graves, V. Hájková, A. Higginbotham, L. Juha, J. Krzywinski, H. J. Lee, M. Messerschmidt, C. D. Murphy, Y. Ping, A. Scherz, W. Schlöter, S. Toleikis, J. J. Turner, L. Vysin, T. Wang, B. Wu, U. Zastrau, D. Zhu, R. W. Lee, P. A. Heimann, B. Nagler, and J. S. Wark, "Creation and diagnosis of a solid-density plasma with an x-ray free-electron laser," *Nature* **482**, 59–62 (2012).
- <sup>7</sup>F.-J. Decker, K. L. Bane, W. Colocho, S. Gilevich, A. Marinelli, J. C. Sheppard, J. L. Turner, J. J. Turner, S. L. Vetter, A. Halavanau, C. Pellegrini, and A. A. Lutman, "Tunable x-ray free electron laser multi-pulses with nanosecond separation," *Sci. Rep.* **12**, 3253 (2022).
- <sup>8</sup>B. Nagler, U. Zastrau, R. R. Faustlin, S. M. Vinko, T. Whitcher, A. J. Nelson, R. Sobierajski, J. Krzywinski, J. Chalupsky, E. Abreu, S. Bajt, T. Bornath, T. Burian, H. Chapman, J. Cihelka, T. Döppner, S. Düsterer, T. Dzelzainis, M. Fajardo, E. Förster, C. Fortmann, E. Galtier, S. H. Glenzer, S. Göde, G. Gregori, V. Hájková, P. Heimann, L. Juha, M. Jurek, F. Y. Khattak, A. R. Khorsand, D. Klinger, M. Kozlova, T. Laarmann, H. J. Lee, R. W. Lee, K.-H. Meiwes-Broer, P. Mercere, W. J. Murphy, A. Przystawik, R. Redmer, H. Reinholz, D. Riley, G. Röpke, F. Rosmej, K. Saksl, R. Schott, R. Thiele, J. Tiggesbäumker, S. Toleikis, T. Tschentscher, I. Uschmann, H. J. Vollmer, and J. S. Wark, "Turning solid aluminium transparent by intense soft x-ray photoionization," *Nat. Phys.* **5**, 693–696 (2009).
- <sup>9</sup>J. Meza-Galvez, N. Gomez-Perez, A. S. Marshall, A. L. Coleman, K. Appel, H. P. Liermann, M. I. McMahon, Z. Konôpková, and R. S. McWilliams, "Thermomechanical response of thickly tamped targets and diamond anvil cells under pulsed hard x-ray irradiation," *J. Appl. Phys.* **127**, 195902 (2020).
- <sup>10</sup>R. J. Husband, R. S. McWilliams, E. J. Pace, A. L. Coleman, H. Hwang, J. Choi, T. Kim, G. C. Hwang, O. B. Ball, S. H. Chun, D. Nam, S. Kim, H. Cynn, V. B. Prakapenka, S.-H. Shim, S. Toleikis, M. I. McMahon, Y. Lee, and H.-P. Liermann, "X-ray free electron laser heating of water and gold at high static pressure," *Commun. Mater.* **2**, 61 (2021).
- <sup>11</sup>N. Hartley, J. Grenzer, W. Lu, L. Huang, Y. Inubushi, N. Kamimura, K. Katagiri, R. Kodama, A. Kon, V. Lipp, M. Makita, T. Matsuoka, N. Medvedev, S. Nakajima, N. Ozaki, T. Pikuz, A. Rode, K. Rohatsch, D. Sagae, A. Schuster, K. Tono, J. Vorberger, T. Yabuuchi, and D. Kraus, "Ultrafast anisotropic disordering in graphite driven by intense hard x-ray pulses," *High Energy Density Phys.* **32**, 63–69 (2019).
- <sup>12</sup>C.-E. Hu, Z.-Y. Zeng, L. Zhang, X.-R. Chen, L.-C. Cai, and D. Alfe, "Theoretical investigation of the high pressure structure, lattice dynamics, phase transition, and thermal equation of state of titanium metal," *J. Appl. Phys.* **107**, 093509 (2010).
- <sup>13</sup>H.-P. Liermann and Z. Jenei, "Kinetics of structural phase transition in the dynamic-diamond anvil cell (dDAC): Bridging static and shock compression," EuXFEL Proposal No. 2592 (2021).
- <sup>14</sup>P. Virtanen, R. Gommers, T. E. Oliphant, M. Haberland, T. Reddy, D. Cournapeau, E. Burovski, P. Peterson, W. Weckesser, J. Bright, S. J. van der Walt, M. Brett, J. Wilson, K. J. Millman, N. Mayorov, A. R. J. Nelson, E. Jones, R. Kern, E. Larson, C. J. Carey, Í. Polat, Y. Feng, E. W. Moore, J. VanderPlas, D. Laxalde, J. Perktold, R. Cimrman, I. Henriksen, E. A. Quintero, C. R. Harris, A. M. Archibald, A. H. Ribeiro, F. Pedregosa, P. van Mulbregt, and SciPy 1.0 Contributors, "SciPy 1.0: Fundamental algorithms for scientific computing in Python," *Nat. Methods* **17**, 261–272 (2020).
- <sup>15</sup>J. Grünert, M. P. Carbonell, F. Dietrich, T. Falk, W. Freund, A. Koch, N. Kujala, J. Laksman, J. Liu, T. Maltezopoulos, K. Tiedtke, U. F. Jastrow, A. Sorokin, E. Syresin, A. Grebentsov, and O. Brovko, "X-ray photon diagnostics at the European XFEL," *J. Synchrotron Radiat.* **26**, 1422–1431 (2019).
- <sup>16</sup>V. Cerantola, A. D. Rosa, Z. Konôpková, R. Torchio, E. Brambrink, A. Rack, U. Zastrau, and S. Pascarelli, "New frontiers in extreme conditions science at synchrotrons and free electron lasers," *J. Phys.: Condens. Matter* **33**, 274003 (2021).
- <sup>17</sup>U. Zastrau, K. Appel, C. Baetz, O. Baehr, L. Batchelor, A. Berghäuser, M. Banjafar, E. Brambrink, V. Cerantola, T. E. Cowan, H. Damker, S. Dietrich, S. D. D. Cafiso, J. Dreyer, H.-O. Engel, T. Feldmann, S. Findeisen, M. Foese, D. Fulla-Marsa, S. Göde, M. Hassan, J. Hauser, T. Herrmannsdörfer, H. Höppner, J. Kaa, P. Kaever, K. Knöfel, Z. Konôpková, A. L. García, H.-P. Liermann, J. Mainberger, M. Makita, E.-C. Martens, E. E. McBride, D. Möller, M. Nakatsutsumi, A. Pelka, C. Plueckthun, C. Prescher, T. R. Preston, M. Röper, A. Schmidt, W. Seidel, J.-P. Schwinkendorf, M. O. Schoelmerich, U. Schramm, A. Schropp, C. Strohmann, K. Sukharnikov, P. Talkovski, I. Thorpe, M. Toncian, T. Toncian, L. Wollenweber, S. Yamamoto, and T. Tschentscher, "The high energy density scientific instrument at the European XFEL," *J. Synchrotron Radiat.* **28**, 1393–1416 (2021).
- <sup>18</sup>T. Maltezopoulos, F. Dietrich, W. Freund, U. F. Jastrow, A. Koch, J. Laksman, J. Liu, M. Planas, A. A. Sorokin, K. Tiedtke, and J. Grünert, "Operation of x-ray gas monitors at the European XFEL," *J. Synchrotron Radiat.* **26**, 1045–1051 (2019).
- <sup>19</sup>A. Allahgholi, J. Becker, A. Delfs, R. Dinapoli, P. Goettlicher, D. Greiffenberg, B. Henrich, H. Hirsemann, M. Kuhn, R. Klanner, A. Klyuev, H. Krueger, S. Lange, T. Laurus, A. Marras, D. Mezza, A. Mozzanica, M. Niemann, J. Poehlsen, J. Schwandt, I. Sheviakov, X. Shi, S. Smoljanin, L. Steffen, J. Sztuk-Dambietz, U. Trunk, Q. Xia, M. Zeribi, J. Zhang, M. Zimmer, B. Schmitt, and H. Graafsma, "The adaptive gain integrating pixel detector at the European XFEL," *J. Synchrotron Radiat.* **26**, 74–82 (2019).
- <sup>20</sup>C. Prescher and V. B. Prakapenka, "DIOPTAS: A program for reduction of two-dimensional x-ray diffraction data and data exploration," *High Pressure Res.* **35**, 223–230 (2015).
- <sup>21</sup>B. Henke, E. Gullikson, and J. Davis, "X-ray interactions: Photoabsorption, scattering, transmission, and reflection at E = 50–30 000 eV, Z = 1–92," *At. Data Nucl. Data Tables* **54**, 181–342 (1993).

- <sup>22</sup>Y. Zhang, Y. Zhao, H. Hou, Z. Wen, and M. Duan, “Comparison of mechanical and thermodynamic properties of FCC and BCC titanium under high pressure,” *Mater. Res. Express* **5**, 026527 (2018).
- <sup>23</sup>O. Senkov, B. Chakoumakos, J. Jonas, and F. Froes, “Effect of temperature and hydrogen concentration on the lattice parameter of beta titanium,” *Mater. Res. Bull.* **36**, 1431–1440 (2001).
- <sup>24</sup>M. W. Chase and N. I. S. O. (US), *NIST-JANAF Thermochemical Tables* (American Chemical Society, Washington, DC, 1998).
- <sup>25</sup>P. J. Linstrom and W. G. Mallard, “The NIST chemistry webbook: A chemical data resource on the internet,” *J. Chem. Eng. Data* **46**, 1059–1063 (2001).
- <sup>26</sup>C. Y. Ho, R. W. Powell, and P. E. Liley, “Thermal conductivity of the elements,” *J. Phys. Chem. Ref. Data* **1**, 279–421 (1972).
- <sup>27</sup>I. Inoue, J. Yamada, K. J. Kapcia, M. Stransky, V. Tkachenko, Z. Jurek, T. Inoue, T. Osaka, Y. Inubushi, A. Ito, Y. Tanaka, S. Matsuyama, K. Yamauchi, M. Yabashi, and B. Ziaja, “Femtosecond reduction of atomic scattering factors triggered by intense x-ray pulse,” *Phys. Rev. Lett.* **131**, 163201 (2023).
- <sup>28</sup>J. Zhang, Y. Zhao, R. S. Hixson, G. T. Gray, L. Wang, W. Utsumi, S. Hiroyuki, and H. Takanori, “Thermal equations of state for titanium obtained by high pressure—temperature diffraction studies,” *Phys. Rev. B* **78**, 054119 (2008).
- <sup>29</sup>C. W. Greeff, D. R. Trinkle, and R. C. Albers, “Shock-induced  $\alpha$ - $\omega$  transition in titanium,” *J. Appl. Phys.* **90**, 2221–2226 (2001).
- <sup>30</sup>E. Y. Tonkov and E. G. Ponyatovsky, *Phase Transformations of Elements under High Pressure*, Advances in Metallic Alloys Vol. 4 (CRC Press, Boca Raton, FL, 2005).
- <sup>31</sup>J. D. McHardy, Ph.D. thesis (University of Edinburgh, 2024).